ARTICLE

Quantum Tunneling Induced Optical Rectification and Plasmon-Enhanced Photocurrent in Nanocavity Molecular Junctions

Dean Kos, Daniel R. Assumpcao, Chenyang Guo, and Jeremy J. Baumberg*

ACCESS | Metrics & More | Article Recommendations | SI Supporting Information

ABSTRACT: Molecular junctions offer the opportunity for downscaling optoelectronic devices. Separating two electrodes with a single layer of molecules accesses the quantum-tunneling regime at low voltages (<1 V), where tunneling currents become highly sensitive to local nanometer-scale geometric features of the electrodes. These features generate asymmetries in the electrical response of the junction which combine with the incident oscillating optical fields to produce optical rectification and photocurrents. Maximizing photocurrents requires accurate control of the overall junction geometry and a large confined optical field in the optimal location. Plasmonic nanostructures such as metallic nanoparticles are prime candidates for this application, because their size and shape dictate a consistent junction geometry while strongly enhancing the optical field from incident light. Here we demonstrate a robust lithography-free molecular optoelectronic device geometry, where a metallic nanoparticle on a self-assembled molecular monolayer is sandwiched between planar bottom and semitransparent top electrodes, to create molecular junctions with reproducible morphology and electrical response. The well-defined geometry enables predictable and intense plasmonic localization, which we show creates optical-frequency voltages ~ 30 mV in the molecular junction from $100\ \mu$W incident light, generating photocurrent by optical rectification (>10 μA/W) from only a few hundred molecules. Quantitative agreement is thus obtained between DC- and optical-frequency quantum-tunneling currents, predicted by a simple analytic equation. By measuring the degree of junction asymmetry for different molecular monolayers, we find that molecules with a large DC rectification ratio also boost zero-bias electrical asymmetry, making them good candidates for sensing and energy harvesting applications in combination with plasmonic nanomaterials.
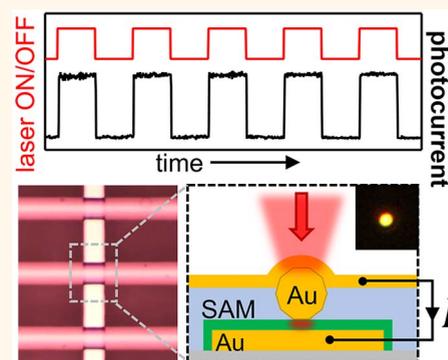
KEYWORDS: molecular electronics, photocurrent, plasmonics, nanoparticle, self-assembly, photodetector

M olecular electronics holds the promise of ultimate circuit miniaturization, where single or few molecules perform electronic functions at the nanometer and sub-nanometer scale, with adaptable functionality and potential gains in energy efficiency, circuit density, and speed.[1] Fundamental aspects of molecular junctions have been extensively explored over the past few decades with a range of benchmark techniques including scanning probe microscopy, mechanical break junctions, and liquid alloy contacts. Supported by increasingly refined theoretical and computational models, these methods have unveiled the fundamental properties of transport through various types of molecules and identified the role of molecular orbitals, chemical functional groups, and molecule−electrode interfaces.[2−4]

At the same time, considerable effort has been put into the design and fabrication of molecular electronic devices,

generally built from fixed electrodes bridged by an ensemble of molecules.[5] Producing devices on the basis of molecular junctions however has proved challenging, as seen in the large number of approaches including growing electrodes through nanopores,[6] deposition of 2D materials,[7] coating with conductive polymers,[8] trapping within nanoparticle networks,[9] and immersion in electrochemical environments[5,10] among others. Despite these efforts many challenges still remain, such

A

as forming junctions with a reproducible number of molecules and preserving molecular integrity during device processing, all while using simple and scalable fabrication methods and geometries that allow for exploiting the properties of small molecular ensembles.

One class of devices that exploits molecular junctions are metallic nanogap antennas, where incident light triggers electrical charge transport across the junction gap amplified by plasmon-enhanced electromagnetic fields. Nanogap antennas have attracted strong interest in recent years for optical detection and energy harvesting[11,12] and light generation,[13] but production of photocurrent from nanogaps has been particularly hard to control consistently due to poor definition of the optical confinement, preventing quantification of the local optical fields.[14,15]

Here we demonstrate an advantageous molecular junction geometry for molecular optoelectronics, where a monolayer of molecules is trapped between a single Au nanoparticle (AuNP) and a flat Au surface integrated within a layered electrode structure. This electrically contacted junction is optically accessible and the AuNP in this nanoparticle-on-mirror (NPoM) geometry[16] serves the double purpose of defining the junction area and plasmonically enhancing the optical field in the gap by several hundred-fold. Upon illumination, local nanoscale asymmetries within the junction produce optical rectification, detected as a photocurrent signal that is boosted by plasmon oscillations in the NPoM structure. Molecules enable the functionality of these devices by defining the nanometer-sized tunneling gap and are used here to evaluate the contribution of various molecular parameters to junction asymmetry.

RESULTS AND DISCUSSION

The nanogaps are formed by depositing AuNPs on a bottom Au electrode patterned on a SiO_2 or glass substrate which has been coated with a self-assembled molecular monolayer (SAM) (Figure 1a). The AuNPs are partially embedded in an insulating PMMA layer, leaving the top half of the NPs exposed, and finally this exposed region is coated with a semitransparent Au film (50% transmission in the visible) to create a top electrode. The intermediate PMMA layer prevents electric contact between the electrodes away from the NPs. The bottom and top Au electrodes are patterned by evaporation through a pair of custom-designed shadow masks (therefore without lithography), so the SAM is never exposed to photoresist, solvents, or UV light. The shadow mask geometries create arrays of approximately 300 cross-bar junction devices per sample (Figure 1b,c, of area 600−2500 μm^2 depending on the device, each containing a few AuNP junctions), which are electrically addressed individually by contacting the corresponding pair of bottom/top electrodes via two external probes. The probes are in turn connected to a function generator, source-measure unit (SMU) or lock-in amplifier depending on the measurement. AuNPs are deposited by drop-casting a colloidal NP solution, with average NP number density within the junctions controlled by NP solution concentration and deposition time. These parameters are tuned to obtain on average 1−10 NPs within the device area, with AuNPs of diameter 100 nm used for all samples here unless otherwise noted. AuNPs are nominally spherical but always partially faceted,[17] and thus trap a few thousand molecules in the planar junction underneath[18] while maintaining tight SAM packing. SAM formation and

uniformity in NPoM geometry has been verified extensively in previous work via large data sets of dark-field and Raman spectroscopy.[16,18] When fabrication is completed, AuNPs within the junctions can be clearly identified with a microscope in dark-field configuration and optically addressed individually for spectroscopy or laser illumination.

To confirm that our device geometry creates working molecular junctions, we verify that device conductance decays exponentially with junction gap size at low DC bias, as expected for junctions in the direct tunneling regime. We systematically fabricate samples using linear alkanedithiol SAMs with chain lengths of 4, 6, 8, and 10 carbon atoms and measure their $I-V$ curves in the ±100 mV range (linear response region) to extract the conductance $G = I/V$ from linear fits to the data (Supporting Information (SI) Figure S1). For each molecule we collect conductance values from ≈100 individual devices into a logarithmic conductance histogram (Figure 1d for 6C chain). In all histograms we observe one prominent conductance peak, sometimes accompanied by other minor peaks or shoulders with sparser density distributions. We fit each set of conductance data with a Gaussian mixture model and assign the weighted mean of the conductance peaks as the characteristic conductance of devices fabricated with that molecule (SI Figure S1). The typical device yield is 40−60% and as high as 85% in some samples (yield measured as percent of junctions per sample that are not shorted and with nonzero conductance). This compares favorably with other small-area ensemble molecular junction geometries,[19] where yields reach 20−70% but without optical access. Device conductance is largely independent of the number of NPs each junction contains, suggesting that only one NP per cross-bar determines the electrical response (SI Figure S2) as verified below.

Plotting the characteristic conductance against the size of the junction gap (Figure 1e), we observe the expected exponential decay typical of direct tunneling. From an exponential fit to the conductance vs gap size d of form $e^{-\beta d}$ we obtain a decay constant $\beta = 4.9 \pm 0.7$ nm^{-1} or $\beta = 0.61 \pm 0.09$ per CH_2 unit, slightly lower than $\beta = 0.8-1.0$ per CH_2 unit often reported in literature.[20] Taking our value of conductance for an 8C chain device and assuming a single molecule conductance[21] of 5nS and that molecules are connected in parallel, from conductance we estimate that on average ~400 molecules contribute to electrical current in each junction. A 100 nm AuNP with a $w = 50$ nm facet diameter (as typically observed[17]) accommodates ~9000 molecules (with 0.21 nm^2/molecule[21]), so only $f \sim 5\%$ of the molecules underneath one NP are effectively contacted and contribute to junction conductance. This is typical of many previous ensemble junctions (e.g., nanopores) since not all molecules are connected at both ends, attributed previously to surface roughness.[21] One advantage of our device geometry is that this number can be tuned by changing the NP diameter D. By fabricating junctions with smaller NPs ($D = 60-100$ nm) the device conductance can be reduced by almost an order of magnitude (Figure 1f), with a power law dependence extracted, $G \propto D^{2.9}$. This exactly matches the scaling of the facet area (Figure 1f dashed line; note facet diameter decreases faster than NP diameter,[17] as validated by Raman measurements). Smaller NPs than $D < 60$ nm become hard to observe optically (scattering strength decreases as D^6). Extrapolating G down to NP diameters of 2−3 nm, which are predicted to have contact facet areas comparable to the size of a molecule, we

obtain a conductance value ~1 nS. This is indeed compatible with the conductance G_m of a single molecule (although Coulomb blockade effects may occur in that regime). These results therefore demonstrate an effective strategy to tune junction conductance over several orders of magnitude, in static and reproducible devices.

The thin top electrode of our devices allows optical access to molecular junctions underneath each individual AuNP. Tight confinement and large field enhancement, enabled by plasmonic coupling between the AuNP and underlying Au surface, strongly amplify the optical fields under the NP within the molecular junction gap,[16] which is the region responsible for electric conduction. In a classical picture, light in the gap is modeled as an AC field $V_{AC}(t) = V_{opt} \cos \omega t$ oscillating at optical frequency ω with amplitude V_{opt}. In the presence of an external DC bias V_{DC} and within a simplified quasistatic approximation, where charges can tunnel through the junction fast enough to follow the optical field, the total current can be expanded to second order as[22]

$$I(t) \simeq I|_{V_{DC}} + \left.\frac{dI}{dV}\right|_{V_{DC}} V_{opt} \cos \omega t + \frac{1}{2}\left.\frac{d^2I}{dV^2}\right|_{V_{DC}} V_{opt}^2 \cos^2 \omega t$$

$$= I_0 + I' \cos \omega t + \frac{1}{4}I'' V_{opt}^2 \cos 2\omega t + \frac{1}{4}I'' V_{opt}^2 \qquad (1)$$

An optical field in the gap can thus generate a net DC photocurrent, $I_{opt} = I'' V_{opt}^2/4$, if the junction has a nonzero I'' nonlinearity, even at zero bias where $V_{DC} = 0$ and therefore $I_0 = 0$. A nonzero I'' can originate from local nanoscale asymmetries within the junction area, such as roughness features or protrusions.[23,24,22] These asymmetries give rise to potential barriers of slightly different shapes in the two directions,[25] so electron tunneling rates are different for positive and negative voltages resulting in asymmetric $I-V$ response and nonzero I'' (see below). Note that this electrical nonlinearity I'' differs from any optical nonlinearities such as multiphoton absorption (which are not seen here since all effects are linear in laser power).

Individual NPoM junctions are first illuminated with an intensity-modulated 633 nm laser, and the resulting device photocurrent detected with lock-in amplification at the modulation frequency. Devices used for photocurrent measurements are fabricated on glass to prevent spurious signals that can originate from Si substrates. Initially we work at zero DC bias and use either 1,6-hexanedithiol (6Cdt), 1,8-octanedithiol (8Cdt), or 1,10-decanedithiol (10Cdt) as molecules for the SAM. When the focused laser beam is positioned on top of a NPoM junction, photocurrent signals are observed only when the laser is on (Figure 2a), and these rapidly decay as the focal spot is moved away from the NP (Figure 2b). This confirms that the NPoM is the only active region of the device. Even when there are several NPs within the device area and each is individually illuminated under the same conditions, we detect photocurrent from one NP only and find no measurable signal in any other location. This active NP is likely the one whose local interface with the bottom electrode results in the largest conductance and junction asymmetry, therefore dominating the others and determining the overall electrical properties of the device. We assign an upper bound to the photocurrent response time of <10 ms, which is the minimum lock-in time constant below which the signal falls below noise.

The photocurrent under continuous laser illumination remains stable for minute time scales as long as the average optical power does not exceed 0.3 mW. Above 0.3 mW, for many junctions we observe fluctuations, flips in direction, and large photocurrent intensities, typically accompanied by a permanent increase in conductance and I'' or even electrical shorts (arising from light-induced welding). To extract the power dependence of the photocurrent, the responsivity is measured when changing the average laser power while maintaining constant (small) power modulation amplitude. We obtain a constant responsivity for low power, indicating a linear power dependence up to ~0.3 mW (Figure 2c), which is disrupted at higher power when changes in junction morphology permanently alter conductance and I''.

To confirm that the measured photocurrent signal originates from optical rectification, we verify the correlation between photocurrent and (near) DC electrical nonlinearity I'' for a set of devices. In this case I'' is measured directly by applying a small AC voltage modulation across each device junction and recording the resulting second-harmonic current with a lock-in amplifier. Comparing the conductance and I'' of each device before and after photocurrent measurements allows laser damage to be identified and these data to be discarded. We observe a positive correlation between optical responsivity and I'' (Figure 2d) over a range of I'' spanning almost 2 orders of magnitude, confirming the origin of the photocurrent from optical rectification set by the junction asymmetry I''. From a linear fit to the data in Figure 2d we obtain $V_{opt}^2 = 0.0075$ V^2/mW, which for the average laser power of $P = 0.1$ mW mostly used in our experiments gives a typical optically induced voltage in the gap of $V_{opt} = 28$ mV corresponding to an electric field in the gap of $\sim 6 \times 10^7$ Vm^{-1}mW$^{-1/2}$, comparable to previous reports for nanoscale plasmonic junctions.[26] The precise plasmonic geometry here provides a strong advantage in allowing a quantitative comparison. Prior theory[16] gives $V_{opt} = dFE_0$ for incident field $E_0 = \sqrt{8P/(c\varepsilon_0\pi s^2)}$, with illumination laser spot diameter $s = 1.5$ μm, plasmonic near-field enhancement $F \sim 200$, and gap size $d \sim 1.2$ nm. This gives estimated $V_{opt} \sim 49$ mV, in good agreement with the experiments. We note that the resulting optically generated fields can easily exceed the breakdown field of molecules.

A thermal origin of the observed photocurrent can be ruled out because continued heating from the laser would establish a steady-state temperature gradient across the molecular gap, resulting in a DC thermal current that would be simply proportional to junction conductance, whereas we observe no correlation between photocurrent intensity and device conductance. Additionally, plasmon oscillations excited by the laser would heat up the NP considerably more than the underlying Au electrode, the former being surrounded by a relatively insulating polymer compared to the large bottom electrode that dissipates heat. A thermoelectric current of this origin would therefore always be directed from the NP toward the bottom electrode, whereas we observe photocurrents in both directions with approximately equal occurrence rates. The typical Seebeck coefficient of alkanedithiol junctions $S = 5$ μV/K[27] would imply a temperature differential of $\Delta T = 5600$ K from thermoelectric effects via $V_{th} = S\Delta T$ to match the 28 mV potential from optical rectification. This would rapidly melt the NP, damage the SAM, and disrupt the junction.

We attribute the dispersion of data points in Figure 2d to a mismatch between the location of plasmonic hotspots underneath the NP (Figure 2d inset) and the position of the nanoscale features that generate electrical asymmetry. The
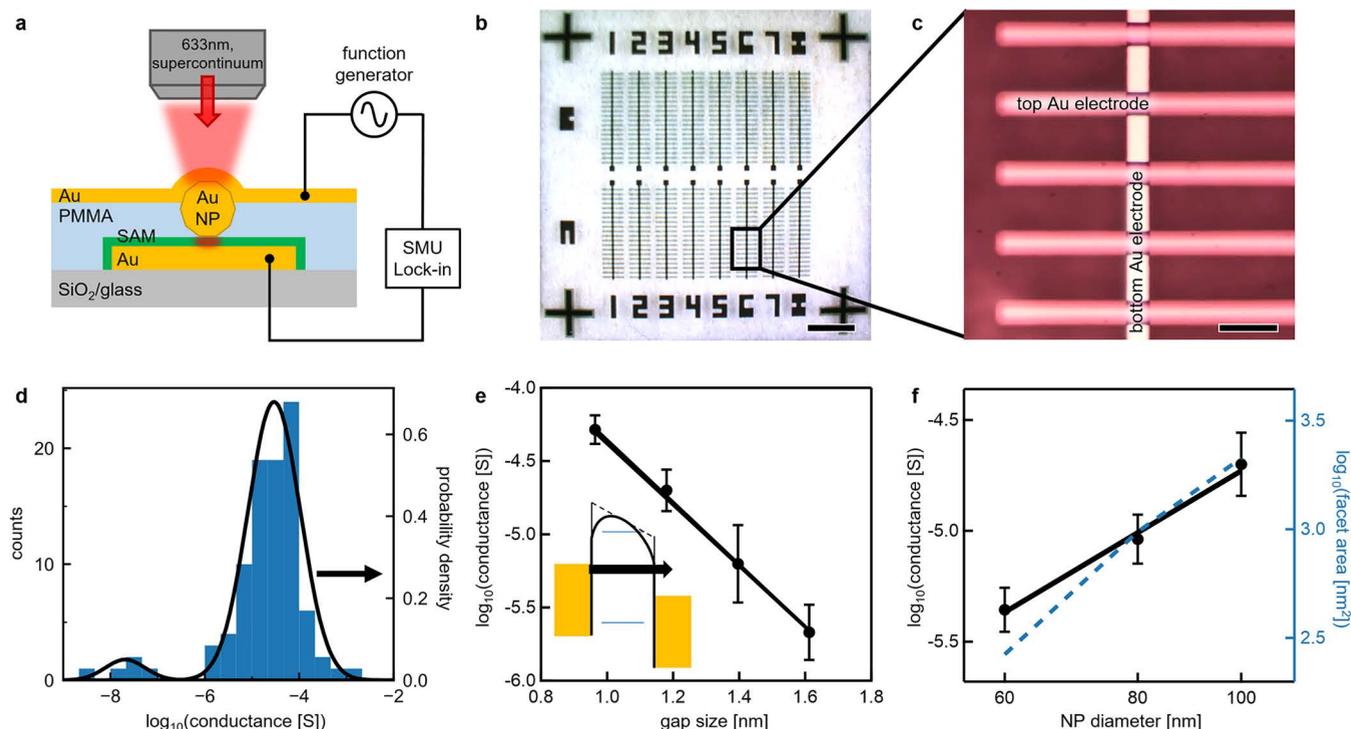
Figure 1. Device geometry and electrical characterization. (a) Molecular junctions formed by SAM sandwiched between bottom Au electrode and AuNP, contacted to semitransparent top Au electrode. (b, c) Top and bottom electrodes arranged to form 300 individual cross-bar devices per sample (scale bars: 2 mm in panel b; 100 μm in panel c). (d) Conductance histogram of 94 junctions made with 1,6-hexanedithiol SAM and 100 nm AuNPs. (e) Conductance decays exponentially with gap size using increasingly long alkanethiols. The line is an exponential fit to the data. (f) Device conductance is tuned by NP size. The solid line is a power law fit to the data; the dashed line shows the facet area. Error bars in panels e and f are standard error of the conductance mean.

main NPoM plasmon-coupled mode is centered at the middle of the NP bottom facet, with a lateral intensity full width at half-maximum (fwhm) of $\sqrt{Dd/\varepsilon_g} \approx 9$ nm (ε_g gap refractive index),[16] while higher order modes have intensity maxima and nodes distributed across the facet area, depending on its exact shape (as in inset Figure 2d). The overlap of local geometric asymmetries and regions with highest optical field determine the overall photocurrent, introducing some variability compared to the electrically measured value of I'', which integrates the 5% contacted molecules and asymmetries over the whole junction facet.

To further confirm the plasmonic enhancement of the photocurrent, its wavelength dependence is measured by illuminating a NP junction with a spectrally filtered super-continuum laser source (spectral bandwidth 20 nm). The photocurrent signal matches well the dark-field scattering spectrum of the same NPoM (Figure 2e), which shows the plasmonic modes of the polymer-coated NPoM system.[16] This allows us to record both the near-field (photocurrent) and far-field (scattering) spectra on the same nanostructure, using plasmon-enhanced optical rectification.

One mechanism to consider is the generation of hot carriers through decay of surface plasmon polaritons.[28−30] In NPoMs, hot carriers would come predominantly from the nanogap and thus the resulting current would have no preferential direction; it would not scale with d^2I/dV^2, and would be asymmetric in voltage since electrons or holes are responsible for transport depending on bias polarity and have different hot carrier energy distributions. The observed spectral dependence of photocurrent can thus be assigned to the increased optical field

in the junction gap near the plasmonic resonance, rather than to generation of hot carriers.

Photocurrents under nonzero DC bias follow the voltage dependence expected from $I''(V)$ (Figure 2f). $I''(V)$ is measured directly through second harmonic lock-in detection at nonzero bias, and in our devices it is typically linear at very low bias $V < 0.05$ V while showing a saturation behavior for $V \geq 0.1$ V, as previously reported for many types of nanogap junctions.[31] The expected photocurrent of an individual junction at nonzero bias is calculated from $I_{opt}(V) = I''(V) V_{opt}^2/4$, where V_{opt} is extracted from the photocurrent and I'' at $V = 0$. The measured and calculated photocurrents are in good agreement (Figure 2f), confirming the photocurrent originates from optical rectification. Operating the junction at $V > 50$ mV boosts the responsivity by over an order of magnitude compared to zero bias, so this regime is most promising for detection applications.

In all junctions considered so far, symmetric alkanedithiol molecules are used that bind to Au electrodes on both ends via thiol functional groups. This implies that the molecules themselves do not contribute significantly to junction asymmetry and I'' originates primarily from local roughness features at the upper/lower molecule−electrode interfaces. This is supported by I'' measurements on many 8Cdt junctions (Figure 3a), showing the distribution of asymmetry parameter at zero bias for different junctions. This reveals that for ∼50% of junctions, conduction is favored toward the substrate and ∼50% toward the NP (Figure 3b). These geometric asymmetries do not translate into DC rectification, measured as $\rho_m = |I(V_m)/I(-V_m)|$ at $V_m = 0.5$ V, which is close to 1 for all junctions (Figure 3c). Fully symmetric molecules such as
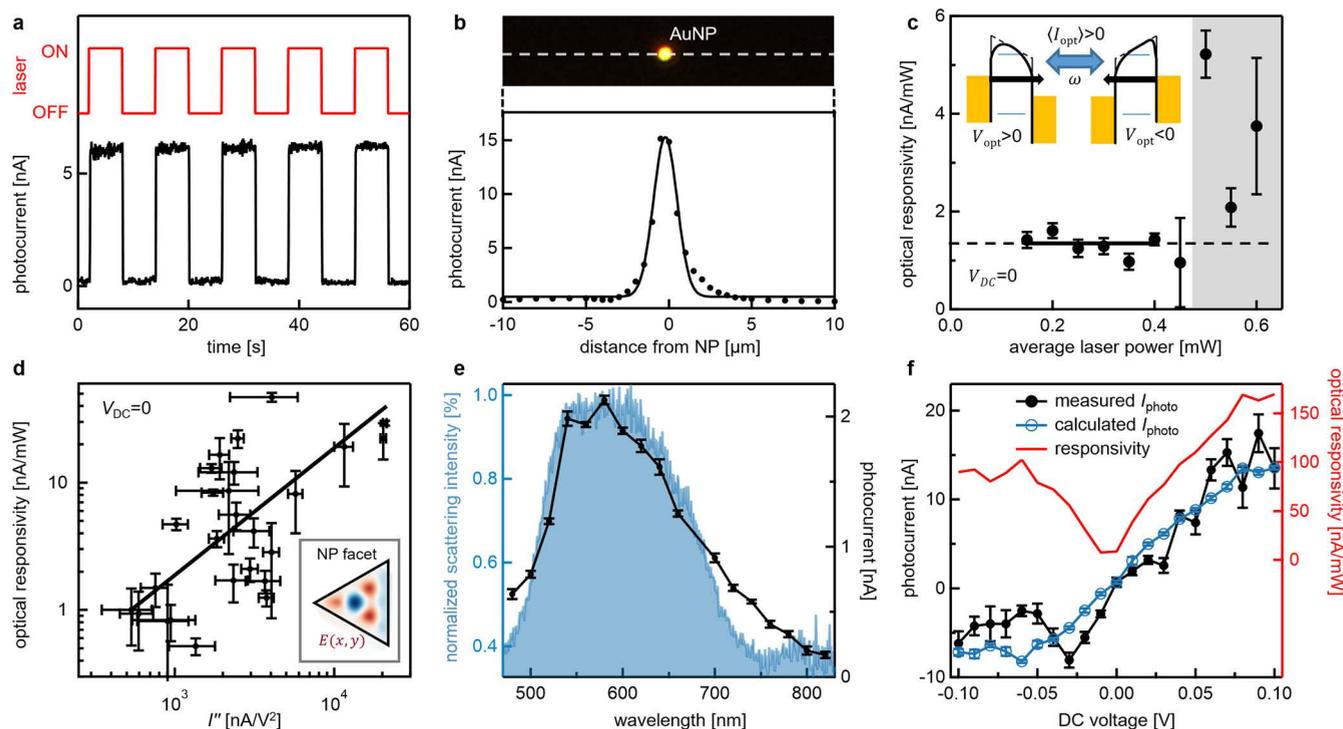
Figure 2. Photocurrents in NPoM molecular devices. (a) Laser at 633 nm, exciting photocurrent when illuminating a single NPoM junction. (b) Photocurrent signal localized to a single AuNP within the device. The line is a Gaussian fit with fwhm = 1 μm. (c) Responsivity (constant at low laser power), with large fluctuations and permanent changes in the junction at higher powers. The insets show optical-frequency tunneling with direction-dependent potential profiles that give rectification. (d) Photocurrent *vs* junction asymmetry I''. The line gives a linear fit, the average laser power is 0.1 mW, the inset shows the mid-gap optical near-field across a triangular junction facet from simulations. (e) Photocurrent wavelength dependence follows scattering spectrum of AuNP junction, indicating plasmonic enhancement of the photocurrent. The average laser power is 25 μW for all wavelengths. (f) Photocurrent measured under DC bias, matching predicted magnitude from $I''(V)$, with responsivity increasing 20-fold from 0 to 0.1 V. The average laser power is 80 μW.

8Cdt mainly define the gap size and geometry, in a way similar to the role of vacuum or air in previous reports of photocurrent detection in nanoscale metallic gaps.[32−34]

When the thiol group on the NP side is replaced by an amine (8-amino-1-octanethiol, 8Cat), the rectification ratio remains close to 1 (Figure 3g), but 72% of junctions now favor conduction toward the bottom electrode (Figure 3f). Even though I'' for 8Cat is on average smaller than for 8Cdt (Figure 3a,e), once I'' is normalized by junction conductance to obtain the *electrical responsivity* ER = I''/I', the contribution to junction responsivity is slightly higher for 8Cat than for 8Cdt (Figure 3d,h). By comparison, using a ferrocene-based alkanethiol (Fc6Ct) gives DC rectification ratios > 1, as expected for this type of molecule[35,36] (Figure 3k), with 84% of junctions favoring conduction toward the bottom electrode (Figure 3j). Significantly, even though the average I'' is smaller than for 8Cdt and 8Cat (Figure 3i), the average electrical responsivity is now almost an order of magnitude larger (Figure 3l). Maximizing electrical responsivity is important for detection applications because it is proportional to the rectified voltage and quantum efficiency of rectification.[22,37]

Photocurrent measurements on Fc6Ct show that indeed the same light-induced tunneling mechanism operates (SI Figure S3). In the simplest model ER = $I''/I' \simeq 2V_m^{-1}(\rho_m - 1)/(\rho_m + 1)$), thus linking the rectification ratio with the plasmon-enhanced optical rectification, although this typically over-estimates the measured values (SI Section SA). Experimentally we find ER = 0.1−1 fluctuates between different junctions. The *optical responsivity* is then given by $I_{opt}(V)/P = I''(V) \times$

$2(dF)^2/(c\varepsilon_0 \pi s^2) = \mathrm{ER}(V) \ 2I'(Fd/s)^2/(\pi c\varepsilon_0)$. Since the field enhancement in the NPoM geometry is known and can be approximated[11] as $F^2 \sim 40 n_g D^2/d^2$ (for gap refractive index of n_g) while $I' \simeq G_m f(w/a)^2[1 + VG'/G]$ where $a \sim 1$ nm is the effective separation of molecules, we can thus estimate the magnitude and scaling of the optical responsivity as

$$\frac{I_{opt}(V)}{P} \sim 2.10^3 \mathrm{ER}(V) n_g \left(\frac{wD}{sa}\right)^2 f G_m \quad (2)$$

Using the parameters noted above, we thus predict $I_{opt}(V)/P \sim$ 20 nA/mW, which is indeed comparable to what is measured (Figure 2f). This gives insight into how to optimize the photocurrent response, which requires high molecular conductance and large electrical responsivity, and as noted above, this is best at higher voltage. However, when a DC voltage is applied, a background tunneling current is produced which has to be distinguished from the photocurrent and creates additional shot detector noise, limiting the optimal bias that can be applied. It is thus crucial to provide the largest ER(V) at the smallest voltage.

Ferrocene-based molecules are widely known to be better rectifying because their ferrocene component, whose HOMO level is just below the Au Fermi energy, introduces an intermediate energy level that allows transport by sequential hopping-tunneling in one direction while only direct tunneling is possible with opposite bias.[35] Detailed studies of the transport mechanism in these molecules have shown that large rectification ratios are generally associated with tight SAM packing, optimal van der Waals molecule−electrode coupling,
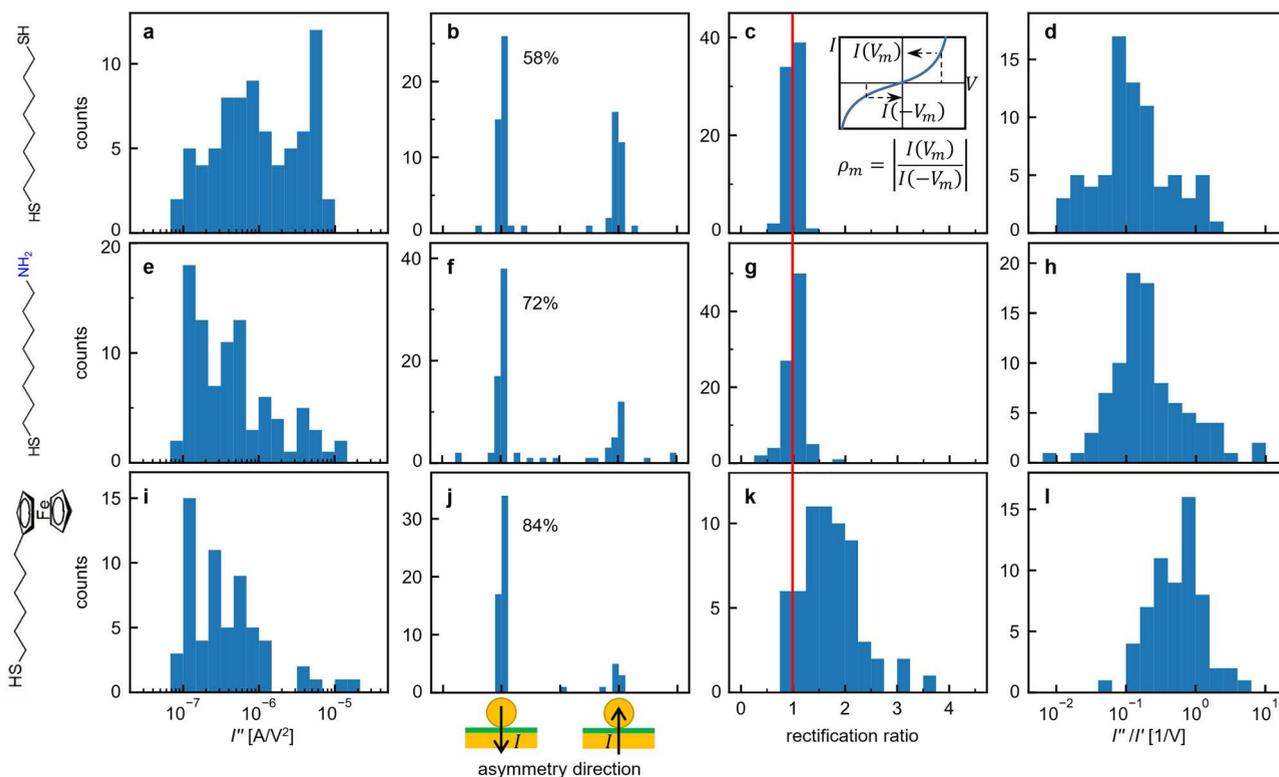
Figure 3. Role of molecules in rectification and junction asymmetry. (a) Histograms from different NPoMs of the zero-bias asymmetry I''. (b) Direction of current flow, current toward bottom electrode corresponding to the lock-in phase $-\pi/2$ and toward NP to phase $+\pi/2$. (c) Rectification ratio (1 for no rectification). (d) Electrical responsivity (ER). The fully symmetric molecule 8Cdt produces junctions with electrical asymmetry evenly distributed between the direction toward AuNP or bottom Au electrode and shows no DC rectification. (e–h) Amine group in 8Cat favors current flow toward the bottom electrode but is also not rectifying and does not significantly affect the magnitude of asymmetry. (i–l) Fc6Ct, a DC rectifying molecule, further enhances directionality and boosts junction asymmetry. $V_m = 0.5$ V for 8Cdt and 8Cat, $V_m = 1$ V for Fc6Ct.

and minimal presence of defects on electrodes.[36] If sequential tunneling was responsible for increased transport asymmetry in our junctions, we would therefore anticipate devices with larger rectification ratio to also show larger responsivity. However, we observe no correlation of rectification ratio with optical responsivity or I'', suggesting that the increased junction asymmetry is not caused by a change in the type of molecular transport through the junction.

Two effects are likely responsible. Sequential tunneling would be slower than direct tunneling, and thus unable to follow the field at optical frequencies. In addition, the 0.1 V modulation amplitude used to directly measure I'' is insufficient to reach the molecular HOMO and trigger sequential tunneling. To explain the symmetry breaking from Fc6Ct, we instead propose that van der Waals interactions of the top NP electrode with Fc6Ct, which is more physisorbed than the chemisorbed S−Au at the bottom electrode, aid restructuring of the molecule−electrode interface upon NP deposition and favor formation of protrusions in the top electrode (Figure 4a). The amine group on 8Cat, which also binds less strongly than thiols, has a similar effect but with reduced magnitude given the linear chain that maintains SAM packing, supporting previous reports on electrical properties of molecular junctions with asymmetric functional groups.[38] By contrast 8Cdt does not introduce asymmetries in interface restructuring and thus shows the smallest responsivity and little directionality (Figure 4b). We note the asymmetry of 8Cat and Fc6Ct and of their molecule−electrode interfaces might also

create an asymmetric tunneling barrier leading to asymmetries in tunneling currents. Additional experiments on a wider range of molecules are needed to develop this model, but it suggests the optimization of optical tunneling photocurrents has to focus on maximizing molecule−electrode binding geometry asymmetries, besides enhancing DC rectification ratios.

The suggested origin of the tunneling asymmetry comes from the non-uniform potential shape and electron image charge as it tunnels away from a perturbation with radius of curvature r (Figure 4c).[25,37] As it emerges, the image charge attractive potential is amplified by the curvature, reducing the barrier for tunneling from this side, but has little effect when at the end of the tunneling trajectory from the other planar electrode.

Metal−insulator−metal (MIM) tunneling junctions have been utilized as photodetectors,[31,39−41] because their "rectenna" response is independent of wavelength, as seen from eq 2, which can now be used to estimate the efficiency of such sub-wavelength-scale tunneling detectors. Typical zero-bias optical responsivities of 20 nA/mW here are lower than those of nanoscale Schottky junctions[42] that can reach 10^6 nA/mW. However, the latter typically operate only in the UV and have microsecond to millisecond response times, whereas the speed of MIM junction detectors is fundamentally limited only by electron tunneling times (typically femtoseconds) and the rectenna RC time constant.[43] Our geometry provides a way to simply reduce the time constant by reducing junction capacitance and resistance with smaller NPs and more

F
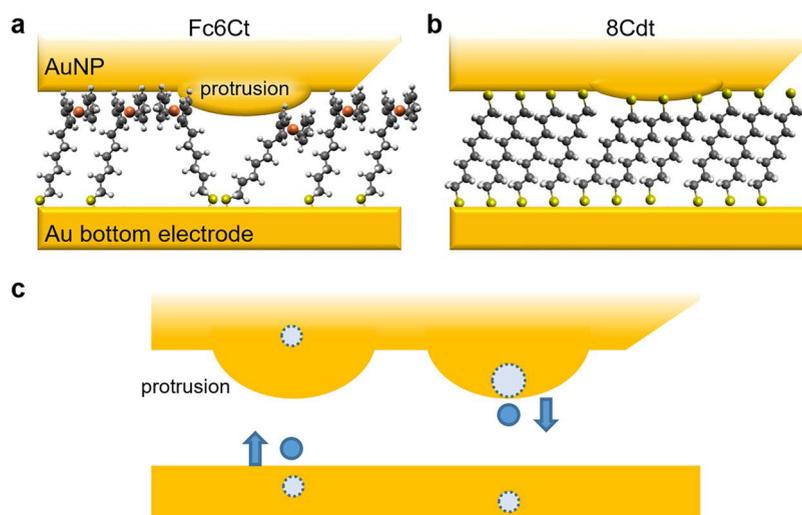
Figure 4. Model for asymmetry and interface restructuring by molecules. (a) Fc6Ct inducing a more significant surface restructuring at the top electrode than (b) symmetric 8Cdt. (c) Image charges of tunneling electrons that are larger when emerging from high-curvature protrusion.

conductive molecules that also boost junction asymmetry. A simple estimate using 20 nm facet width, 1 nm junction gap, and 1 kΩ resistance gives RC ∼ 2 fs (using the gap capacitance),[16] promising for ultrahigh-speed detection in the visible. Conjugated oligophenylene molecules with asymmetric functional groups are likely good candidates to maximize optical responsivity while keeping device resistance low.

The optical responsivity of our alkanedithiol devices at 0.1 V is typically in the 100−200 nA/mW range, similar to alternative plasmonic detectors based on hot electron generation demonstrated for the visible and IR.[44] Electrical responsivity in junctions with Fc6Ct is 0.1−1 V^{-1} at zero bias and 1−5 V^{-1} at 0.1 V, which is already in line with terahertz responsivities of MIM junctions rationally designed to optimize detection in the terahertz regime.[45] Our device geometry could provide an alternative to semiconductor photodetectors for high-speed data transfer in integrated photonic circuits.[46] In terms of energy harvesting applications, the typical electrical power generated by one junction for 0.1 mW optical power is around 10^{-5}mW ($P = V_{opt}^2 G$, with $V_{opt} = 28$ mV and $G = 20$ μS), corresponding to a power conversion efficiency of 10^{-4}. Considering however that the NP diameter is 100 nm, illuminated by a 1.5 μm diameter laser spot, the efficiency for the active device area becomes $\eta = 1\%$. This does not compete with photovoltaic generators but could find applications where device miniaturization and ease of fabrication are critical.

CONCLUSIONS

In conclusion we show that combining reliable plasmonic constructs with self-assembly of molecules provides an effective strategy to create nanometer-sized gaps for sensing and energy harvesting from light. Molecules play a crucial role in defining the transport characteristics of these nanodevices and their resultant optoelectronic properties. Selection of optimal molecules is essential, but those that show large DC rectification ratios are not necessarily the best candidates for optical-frequency rectification at zero bias, due to the molecular transport mechanisms involved. In our devices, an incident optical power of 100 μW can easily generate an AC voltage of tens of millivolts in the plasmonic cavity, while much

higher optical fields disrupt the molecular junction. We derive an estimate for the optical responsivity which matches experiments well. To exploit molecules for optical rectification, they should be designed to display large rectification ratios (at zero or nonzero DC bias) within the safe potential window.

METHODS

Fabrication. Samples for electrical measurements only are fabricated on Si wafer substrates with 500 nm thick thermal SiO$_2$ layer (Si-Mat), while those for photocurrent measurements are deposited on borosilicate glass wafers (Pi-Kem). Fabrication starts with patterning of bottom electrodes by thermal evaporation (NanoPVD-T15A, Moorfield Nanotechnology) of 5 nm of Cr and 30 nm of Au at a rate of 0.1 nm/s through shadow masks (PhotoFab, Alphasol Tec AG). To form a SAM, the sample is immersed overnight in 1 mM solution in ethanol of the molecule of interest (Sigma-Aldrich), *i.e.*, 1,4-butanedithiol (4Cdt), 1,6-hexanedithiol (6Cdt), 1,8-octanedithiol (8Cdt), 1,10-decanedithiol (10Cdt), 8-amino-1-octane-thiol (8Cat), or 6-(ferrocenyl)hexanethiol (Fc6Ct); then washed with ethanol; and blown dry with N$_2$. AuNPs (BBI solutions) are deposited by drop-casting. Poly(methyl methacrylate) (PMMA; molecular weight, 950 kg/mol) at 2 wt % in anisole (MicroChem) is spin-coated at a speed of 2 krpm and 250 rpm/s acceleration and then baked at 50 °C on a hot plate for 2 min, for a final PMMA thickness above the substrate surface of ∼100 nm. PMMA is selectively etched by 25−30 nm using O$_2$ plasma (HPT-100, Henniker Plasma) to expose the top of the AuNPs. Finally top electrodes are patterned by thermal evaporation of 12 nm Au through the shadow mask. Film thicknesses are measured on reference samples using AFM (MFP-3D, Asylum Research) and ellipsometry (Alpha-SE, J.A. Woollam).

Microscopy, Dark-Field Spectroscopy, and Probe Setup. Imaging and dark-field spectroscopy are achieved using a modified BX51 microscope with confocal fiber-coupled spectrometer (QE65000, Ocean Optics) with 1.5 μm acquisition spot diameter. Electrodes on the sample are contacted with tungsten probes (American Probe & Technologies) mounted in a custom probe station integrated with the microscope. All measurements are conducted at room temperature and ambient conditions.

Electrical Measurements. *I−V* curves are acquired with a source-measure unit (2635A, Keithley). *I″* is measured through a function generator (33220A, Agilent) and lock-in amplifier (SR810, Stanford Research Systems) in series with the junction being measured, with lock-in set to second harmonic current detection mode using 500 Hz sine wave modulation with typical amplitude 0.1

V peak-to-peak and zero or nonzero DC offset depending on the measurement.

Photocurrent Measurements. A red laser (633 nm MatchBox series, Integrated Optics) is coupled into the microscope from free space and focused to a 1.5 μm diameter spot on the sample. Laser power is controlled with an acousto-optic modulator and calibrated with a power meter (S120C, Thorlabs) at the sample location. The laser is sine wave modulated at 1 kHz with average optical power of 0.1 mW and peak-to-peak modulation amplitude of 0.1 mW. The modulation is used as reference for the lock-in amplifier in first harmonic current detection mode to measure the photocurrent. For photocurrent spectra the red laser is replaced by a filtered supercontinuum source (Fianium fiber laser, SuperChrome filter unit) with 20 nm fwhm bandwidth calibrated to apply the same optical power on the sample at all wavelengths, modulated by a chopper (MC2000B, Thorlabs) at 788 Hz and with typical average optical power of 0.025−0.05 mW. "Asymmetry direction" in Figure 3b,f,j is obtained from the phase of the signal measured by the lock-in amplifier.

ASSOCIATED CONTENT

ⓢ Supporting Information

The Supporting Information is available free of charge at https://pubs.acs.org/doi/10.1021/acsnano.1c04100.

Additional conductance data for alkanedithiol and ferrocene molecules, AFM data for surface roughness, equation derivations, and simulations of thermal expansion in NPoM junctions (PDF)

AUTHOR INFORMATION

Corresponding Author

Jeremy J. Baumberg − *NanoPhotonics Centre, Cavendish Laboratory, Department of Physics, University of Cambridge, Cambridge CB3 0HE, United Kingdom;* ⓞ orcid.org/0000-0002-9606-9488; Email: jjb12@cam.ac.uk

Authors

Dean Kos − *NanoPhotonics Centre, Cavendish Laboratory, Department of Physics, University of Cambridge, Cambridge CB3 0HE, United Kingdom*

Daniel R. Assumpcao − *NanoPhotonics Centre, Cavendish Laboratory, Department of Physics, University of Cambridge, Cambridge CB3 0HE, United Kingdom*

Chenyang Guo − *NanoPhotonics Centre, Cavendish Laboratory, Department of Physics, University of Cambridge, Cambridge CB3 0HE, United Kingdom*

Complete contact information is available at:
https://pubs.acs.org/10.1021/acsnano.1c04100

Author Contributions

The experiments were devised by D.K., D.R.A., and J.J.B. Sample fabrication and measurements were conducted by D.K., D.R.A., and C.G. The optical responsivity model was developed by J.J.B. The manuscript was written with contributions from all authors.

Notes

The authors declare no competing financial interest.
Experimental data related to figures in the main text and Supporting Information is available free of charge at https://doi.org/10.17863/CAM.74478.

ACKNOWLEDGMENTS

REFERENCES

(1) Does Molecular Electronics Compute? *Nat. Nanotechnol.* **2013**, *8* (6), 377. .

(2) Xiang, D.; Wang, X.; Jia, C.; Lee, T.; Guo, X. Molecular-Scale Electronics: From Concept to Function. *Chem. Rev.* **2016**, *116* (7), 4318−4440.

(3) Ratner, M. A Brief History of Molecular Electronics. *Nat. Nanotechnol.* **2013**, *8* (6), 378−381.

(4) Aradhya, S. V.; Venkataraman, L. Single-Molecule Junctions beyond Electronic Transport. *Nat. Nanotechnol.* **2013**, *8* (6), 399−410.

(5) Vilan, A.; Aswal, D.; Cahen, D. Large-Area, Ensemble Molecular Electronics: Motivation and Challenges. *Chem. Rev.* **2017**, *117* (5), 4248−4286.

(6) Wang, W.; Lee, T.; Reed, M. A. Electron Tunnelling in Self-Assembled Monolayers. *Rep. Prog. Phys.* **2005**, *68* (3), 523−544.

(7) Wang, G.; Kim, Y.; Choe, M.; Kim, T.-W.; Lee, T. A New Approach for Molecular Electronic Junctions with a Multilayer Graphene Electrode. *Adv. Mater.* **2011**, *23* (6), 755−760.

(8) Akkerman, H. B.; Blom, P. W. M.; de Leeuw, D. M.; de Boer, B. Towards Molecular Electronics with Large-Area Molecular Junctions. *Nature* **2006**, *441* (7089), 69−72.

(9) Jafri, S. H. M.; Löfås, H.; Blom, T.; Wallner, A.; Grigoriev, A.; Ahuja, R.; Ottosson, H.; Leifer, K. Nano-Fabrication of Molecular Electronic Junctions by Targeted Modification of Metal-Molecule Bonds. *Sci. Rep.* **2015**, *5* (1), 14431.

(10) Cui, L.; Liu, B.; Vonlanthen, D.; Mayor, M.; Fu, Y.; Li, J.-F.; Wandlowski, T. In Situ Gap-Mode Raman Spectroscopy on Single-Crystal Au(100) Electrodes: Tuning the Torsion Angle of 4,4′-Biphenyldithiols by an Electrochemical Gate Field. *J. Am. Chem. Soc.* **2011**, *133* (19), 7332−7335.

(11) Novotny, L.; van Hulst, N. Antennas for Light. *Nat. Photonics* **2011**, *5* (2), 83−90.

(12) Knight, M. W.; Sobhani, H.; Nordlander, P.; Halas, N. J. Photodetection with Active Optical Antennas. *Science* **2011**, *332* (6030), 702−704.

(13) Kern, J.; Kullock, R.; Prangsma, J.; Emmerling, M.; Kamp, M.; Hecht, B. Electrically Driven Optical Antennas. *Nat. Photonics* **2015**, *9* (9), 582−586.

(14) Shi, S.-F.; Xu, X.; Ralph, D. C.; McEuen, P. L. Plasmon Resonance in Individual Nanogap Electrodes Studied Using Graphene Nanoconstrictions as Photodetectors. *Nano Lett.* **2011**, *11* (4), 1814−1818.

(15) Taychatanapat, T.; Bolotin, K. I.; Kuemmeth, F.; Ralph, D. C. Imaging Electromigration during the Formation of Break Junctions. *Nano Lett.* **2007**, *7* (3), 652−656.

(16) Baumberg, J. J.; Aizpurua, J.; Mikkelsen, M. H.; Smith, D. R. Extreme Nanophotonics from Ultrathin Metallic Gaps. *Nat. Mater.* **2019**, *18* (7), 668.

(17) Benz, F.; Chikkaraddy, R.; Salmon, A.; Ohadi, H.; de Nijs, B.; Mertens, J.; Carnegie, C.; Bowman, R. W.; Baumberg, J. J. SERS of Individual Nanoparticles on a Mirror: Size Does Matter, but So Does Shape. *J. Phys. Chem. Lett.* **2016**, *7* (12), 2264−2269.

(18) Benz, F.; Tserkezis, C.; Herrmann, L. O.; de Nijs, B.; Sanders, A.; Sigle, D. O.; Pukenas, L.; Evans, S. D.; Aizpurua, J.; Baumberg, J. J. Nanooptics of Molecular-Shunted Plasmonic Nanojunctions. *Nano Lett.* **2015**, *15* (1), 669−674.

(19) Jeong, H.; Kim, D.; Xiang, D.; Lee, T. High-Yield Functional Molecular Electronic Devices. *ACS Nano* **2017**, *11* (7), 6511−6548.

(20) Song, H.; Kim, Y.; Jeong, H.; Reed, M. A.; Lee, T. Coherent Tunneling Transport in Molecular Junctions. *J. Phys. Chem. C* **2010**, *114* (48), 20431−20435.

(21) Nichols, R. J.; Haiss, W.; Higgins, S. J.; Leary, E.; Martin, S.; Bethell, D. The Experimental Determination of the Conductance of Single Molecules. *Phys. Chem. Chem. Phys.* **2010**, *12* (12), 2801−2815.

(22) Mayer, A.; Chung, M. S.; Lerner, P. B.; Weiss, B. L.; Miskovsky, N. M.; Cutler, P. H. Classical and Quantum Responsivities of Geometrically Asymmetric Metal-Vacuum-Metal Junctions Used for the Rectification of Infrared and Optical Radiations. *J. Vac. Sci. Technol., B: Nanotechnol. Microelectron.: Mater., Process., Meas., Phenom.* **2011**, *29* (4), No. 041802.

(23) Nguyen, H. Q.; Cutler, P. H.; Feuchtwang, T. E.; Huang, Z.-H.; Kuk, Y.; Silverman, P. J.; Lucas, A. A.; Sullivan, T. E. Mechanisms of Current Rectification in an STM Tunnel Junction and the Measurement of an Operational Tunneling Time. *IEEE Trans. Electron Devices* **1989**, *36* (11), 2671−2678.

(24) Mayer, A.; Chung, M. S.; Weiss, B. L.; Miskovsky, N. M.; Cutler, P. H. Three-Dimensional Analysis of the Geometrical Rectifying Properties of Asymmetric Metal-Vacuum-Metal Junctions and Extension for Energy Conversion. *Phys. Rev. B: Condens. Matter Mater. Phys.* **2008**, *77* (8), No. 085411.

(25) Miskovsky, N. M.; Cutler, P. H.; Feuchtwang, T. E.; Shepherd, S. J.; Lucas, A. A.; Sullivan, T. E. Effect of Geometry and Multiple-image Interactions on Tunneling and I-V Characteristics of Metal-Vacuum-Metal Point-Contact Junctions. *Appl. Phys. Lett.* **1980**, *37* (2), 189−192.

(26) Arielly, R.; Ofarim, A.; Noy, G.; Selzer, Y. Accurate Determination of Plasmonic Fields in Molecular Junctions by Current Rectification at Optical Frequencies. *Nano Lett.* **2011**, *11* (7), 2968−2972.

(27) Wang, K.; Meyhofer, E.; Reddy, P. Thermal and Thermo-electric Properties of Molecular Junctions. *Adv. Funct. Mater.* **2020**, *30* (8), 1904534.

(28) Fung, E.-D.; Adak, O.; Lovat, G.; Scarabelli, D.; Venkataraman, L. Too Hot for Photon-Assisted Transport: Hot-Electrons Dominate Conductance Enhancement in Illuminated Single-Molecule Junctions. *Nano Lett.* **2017**, *17* (2), 1255−1261.

(29) Zolotavin, P.; Evans, C.; Natelson, D. Photothermoelectric Effects and Large Photovoltages in Plasmonic Au Nanowires with Nanogaps. *J. Phys. Chem. Lett.* **2017**, *8* (8), 1739−1744.

(30) Reddy, H.; Wang, K.; Kudyshev, Z.; Zhu, L.; Yan, S.; Vezzoli, A.; Higgins, S. J.; Gavini, V.; Boltasseva, A.; Reddy, P.; Shalaev, V. M.; Meyhofer, E. Determining Plasmonic Hot-Carrier Energy Distributions *via* Single-Molecule Transport Measurements. *Science* **2020**, *369* (6502), 423−426.

(31) Fumeaux, C.; Herrmann, W.; Kneubühl, F. K.; Rothuizen, H. Nanometer Thin-Film Ni−NiO−Ni Diodes for Detection and Mixing of 30 THz Radiation. *Infrared Phys. Technol.* **1998**, *39* (3), 123−183.

(32) Ward, D. R.; Hüser, F.; Pauly, F.; Cuevas, J. C.; Natelson, D. Optical Rectification and Field Enhancement in a Plasmonic Nanogap. *Nat. Nanotechnol.* **2010**, *5* (10), 732−736.

(33) Stolz, A.; Berthelot, J.; Mennemanteuil, M.-M.; Colas des Francs, G.; Markey, L.; Meunier, V.; Bouhelier, A. Nonlinear Photon-Assisted Tunneling Transport in Optical Gap Antennas. *Nano Lett.* **2014**, *14* (5), 2330−2338.

(34) Cui, L.; Zhu, Y.; Abbasi, M.; Ahmadivand, A.; Gerislioglu, B.; Nordlander, P.; Natelson, D. Electrically Driven Hot-Carrier Generation and Above-Threshold Light Emission in Plasmonic Tunnel Junctions. *Nano Lett.* **2020**, *20* (8), 6067−6075.

(35) Yuan, L.; Nerngchamnong, N.; Cao, L.; Hamoudi, H.; del Barco, E.; Roemer, M.; Sriramula, R. K.; Thompson, D.; Nijhuis, C. A. Controlling the Direction of Rectification in a Molecular Diode. *Nat. Commun.* **2015**, *6* (1), 6324.

(36) Thompson, D.; Nijhuis, C. A. Even the Odd Numbers Help: Failure Modes of SAM-Based Tunnel Junctions Probed *via* Odd-Even Effects Revealed in Synchrotrons and Supercomputers. *Acc. Chem. Res.* **2016**, *49* (10), 2061−2069.

(37) Miskovsky, N. M.; Cutler, P. H.; Mayer, A.; Weiss, B. L.; Willis, B.; Sullivan, T. E.; Lerner, P. B. Nanoscale Devices for Rectification of High Frequency Radiation from the Infrared through the Visible: A New Approach. *J. Nanotechnol.* **2012**, *2012*, No. 512379.

(38) Beebe, J. M.; Kim, B.; Gadzuk, J. W.; Daniel Frisbie, C.; Kushmerick, J. G. Transition from Direct Tunneling to Field Emission in Metal-Molecule-Metal Junctions. *Phys. Rev. Lett.* **2006**, *97* (2), No. 026801.

(39) Fumeaux, C.; Alda, J.; Boreman, G. D. Lithographic Antennas at Visible Frequencies. *Opt. Lett.* **1999**, *24* (22), 1629−1631.

(40) Krishnan, S.; La Rosa, H.; Stefanakos, E.; Bhansali, S.; Buckle, K. Design and Development of Batch Fabricatable Metal−Insulator−Metal Diode and Microstrip Slot Antenna as Rectenna Elements. *Sens. Actuators, A* **2008**, *142* (1), 40−47.

(41) Bareib, M.; Tiwari, B. N.; Hochmeister, A.; Jegert, G.; Zschieschang, U.; Klauk, H.; Fabel, B.; Scarpa, G.; Koblmuller, G.; Bernstein, G. H.; Porod, W.; Lugli, P. Nano Antenna Array for Terahertz Detection. *IEEE Trans. Microwave Theory Tech.* **2011**, *59* (10), 2751−2757.

(42) Tian, W.; Wang, Y.; Chen, L.; Li, L. Self-Powered Nanoscale Photodetectors. *Small* **2017**, *13* (45), 1701848.

(43) Grover, S.; Moddel, G. Applicability of Metal/Insulator/Metal (MIM) Diodes to Solar Rectennas. *IEEE J. Photovoltaics* **2011**, *1* (1), 78−83.

(44) Li, W.; Valentine, J. G. Harvesting the Loss: Surface Plasmon-Based Hot Electron Photodetection. *Nanophotonics* **2017**, *6* (1), 177−191.

(45) Gadalla, M. N.; Abdel-Rahman, M.; Shamim, A. Design, Optimization and Fabrication of a 28.3 THz Nano-Rectenna for Infrared Detection and Rectification. *Sci. Rep.* **2015**, *4* (1), 4270.

(46) Mauthe, S.; Baumgartner, Y.; Sousa, M.; Ding, Q.; Rossell, M. D.; Schenk, A.; Czornomaz, L.; Moselund, K. E. High-Speed III-V Nanowire Photodetector Monolithically Integrated on Si. *Nat. Commun.* **2020**, *11* (1), 4565.